Investigation of the Flow Field Characteristics of Aortic Bileaflet Mechanical Heart Valves with Different Leaflet Shapes Using PIV

Y. Qiang[1,2†], T. C. Duan[1,2], M. Z. Zhang[1,2], L. Qi[3] and L. J. Wei[1,2]

[1] *Energy and Power Engineering College, Lanzhou University of Technology, Lanzhou, Gansu Province, 730050, China*
[2] *Key Laboratory of Advanced Pumps, Valves and Fluid Control System of the Ministry of Education, Lanzhou University of Technology, Lanzhou, Gansu Province, 730050, China*
[3] *Cardiovascular Surgery, The First Hospital of Lanzhou University, Lanzhou, Gansu Province, 730000, China*

†*Corresponding Author Email: 20070046@lut.edu.cn*

ABSTRACT

Non-physiological flow patterns generated by bileaflet mechanical aortic valves are closely associated with thromboembolism following valve replacement surgery. Investigating how different leaflet shapes affect the flow field characteristics of these valves can help optimize leaflet designs to improve hemodynamic performance and reduce postoperative complications. This study used clinical CT imaging data to create a realistic silicone model of the aortic root, setting up an extracorporeal pulsatile flow system to simulate cyclical blood flow. Particle image velocimetry was used to capture the periodic flow field downstream of bileaflet mechanical aortic valves with straight and curved leaflets, analyzing the impact of leaflet shape on velocity distribution, vortex dynamics, viscous shear stress (VSS), and Reynolds shear stress (RSS). Results indicate that the curved leaflets reduced the impact on the aortic sinus, mitigating endothelial cell damage caused by high velocity. The curved leaflet design also increased the effective flow area, preventing blood stagnation and reducing local concentrations of coagulation factors, thus lowering the risk of thrombus formation. The maximum VSS for the straight and curved leaflets were 1.93 N/m^2 and 1.87 N/m^2, respectively, while the RSS reached 152 N/m^2 and 118 N/m^2, respectively. Curved leaflets minimized turbulent shear stress on blood cells, reducing platelet activation and lowering the incidence of thromboembolism. Optimizing leaflet curvature offers a promising avenue for enhancing the hemodynamic performance of bileaflet mechanical aortic valves. Curved designs may also be more suitable for older patients or those with reduced cardiac ejection capacity, improving surgical outcomes and recovery.

1. INTRODUCTION

Aortic valve disease, characterized by malformations or degenerative calcification of the valve leaflets, leads to impaired valve function, preventing the proper opening and closing of the aortic valve. This impairment disrupts unidirectional blood flow, ultimately contributing to heart failure in patients (Yang et al., 2021). Prosthetic heart valve (PHV) replacement has emerged as the primary treatment modality for addressing aortic valve pathology. Among PHVs, bileaflet mechanical heart valves (BMHVs) are widely utilized in clinical settings due to their durability (Marquis-Gravel et al., 2016). However, despite the success of aortic valve replacement surgery, clinical outcomes often remain suboptimal, with many complications linked to hemodynamic factors (Garg et al.,

2023). Non-physiological flow patterns can trigger the fragmentation of red blood cells, leading to hemolysis, while stasis of blood flow and platelet activation may precipitate thrombus formation, posing considerable risks for thromboembolic events that threaten cardiovascular health (Kawahito & Nosé, 2008; Selmi et al., 2019).

The design of mechanical heart valves fundamentally shapes their flow field characteristics, and variations in these characteristics, such as high-velocity gradients, recirculation zones, flow stagnation, and elevated shear stress, are strongly correlated with post-surgical complications, including thromboembolism (Rajput & Zeltser, 2023). Therefore, the evaluation of the flow field dynamics of mechanical aortic valves with different leaflet geometries is essential for understanding how valve

Nomenclauture			
PHV	Prosthetic Heart Valve	DUS	Duplex Ultrasound
BMHV	Bileaflet Mechanical Heart Valve	vWf	von Willebrand Factor
PIV	Particle Image Velocimetry	CFD	Computational Fluid Dynamics
Tomo-PIV	Tomographic Particle Image Velocimetry	LDV	Laser Doppler Velocimetry
MRI	Magnetic Resonance Imaging	CT	Computed Tomography
		LV	Left Ventricle

structure contributes to non-physiological flow patterns and postoperative complications, such as thrombosis (Liu et al., 2019; 2020). A clearer comprehension of these mechanisms is vital for enhancing patient survival rates post-surgery and optimizing future valve designs.

Traditional clinical imaging techniques, such as Doppler ultrasound (DUS) and magnetic resonance imaging (MRI), are limited in their spatial and temporal resolution, which constrains their ability to capture detailed flow characteristics-particularly the small-scale features, such as turbulence and vortex shedding that occur around mechanical heart valves. For this reason, optical measurement techniques, such as particle image velocimetry (PIV) and laser Doppler velocimetry (LDV), have become key tools in studying the flow characteristics of aortic valves under in vitro conditions. However, LDV is time-intensive when applied to analyze full-field data across the entire cardiac cycle, while PIV, as a non-invasive full-field technique, offers the advantage of capturing instantaneous velocity fields across an entire flow domain without disturbing the flow, making it an invaluable tool in studies of aortic valve hemodynamics.

The structure and geometry of valve leaflets considerably influence downstream flow characteristics. Differences in valve type, design, and size generate distinct hemodynamic variations (Black & Drury, 1994; Chandran et al., 1985; Knoch et al., 1988). In the 1970s, St. Jude Medical (SJM) developed the first BMHV, which was successfully implanted in clinical settings in 1977 (Horstkotte et al., 1981). Subsequent experimental studies have shown that bileaflet valves offer reduced flow resistance and lower rates of thromboembolic complications compared to other designs, such as ball-and-cage or trileaflet valves, owing to the smaller projection area of the occluder. These valves also boast a larger effective orifice area, making them more efficient (Chew et al., 1993; Linde et al., 2012; Hatoum et al., 2022).

Grigioni et al. (2001) used LDV to investigate the flow velocity and Reynolds shear stress (RSS) in BMHVs with flat and curved leaflets. They found that curved leaflets resulted in both stable and unstable regions downstream, where leaflet curvature influenced turbulent shear stress, with the convex side of the leaflet experiencing lower turbulence intensity than the concave side. However, their study did not include ensemble-averaged measurements or capture full-field optical data (Grigioni et al., 2001).

Akutsu & Fukuda (2005), Akutsu & Saito (2006), Akutsu, et al. (2008), and Akutsu & Matsumoto (2010) utilized PIV under pulsatile flow conditions to compare the flow fields of four bileaflet valves: 29-mm SJM flat valves, 27-mm On-X flat valves, 27-mm Jyros (JR) curved valves, and 27-mm Edwards MIRA curved valves. Their study examined how leaflet shape and valve design influence velocity distribution and turbulent shear stress. The high-resolution, dynamic PIV approach enabled the capture of real-time flow and turbulence data, revealing that small variations in leaflet design can lead to substantial differences in flow behavior. The SJM, On-X, and MIRA valves exhibited higher central orifice velocities, whereas the JR valve, with its curved leaflets, produced higher velocities and more divergent flow patterns during the

acceleration and peak flow phases. The JR valves generated substantially higher turbulent stresses than the SJM valves. However, the study did not capture the symmetric flow in the left and right aortic sinuses, and an elastic artery model was not used, limiting the ability to replicate the effects of arterial compliance on transvalvular flow.

In summary, BMHVs demonstrate superior flow efficiency and lower transvalvular pressure gradients compared to other valve designs. However, complications arising from non-physiological flow patterns persist due to structural differences between mechanical and native valves. Current studies have largely used rigid, idealized models of the aortic root, failing to account for arterial compliance effects on transvalvular flow. Furthermore, most experimental studies only capture flow data at isolated points within the cardiac cycle without full-field optical measurements of downstream flow dynamics. As a result, there remains a lack of detailed, periodic flow field data for assessing how different leaflet geometries influence the downstream flow characteristics of BMHVs under pulsatile flow conditions.

This study addresses this gap by reconstructing 3D models of the aortic root and left ventricle (LV) using clinical cardiac CT data and employing 3D printing to create flexible, transparent silicone models of the aortic root. An extracorporeal pulsatile flow system was developed to simulate periodic blood flow, with adjustable pressure chambers replicating arterial compliance. PIV was used to investigate the flow field characteristics downstream of BMHVs with flat and curved leaflets, focusing on velocity distribution, vortex evolution, viscous shear stress (VSS), and RSS. The results provide critical data for optimizing valve selection and design in clinical aortic valve replacement surgeries.

2. MATERIALS AND METHODS

2.1 Experimental Model

This study utilized clinical data from the First Affiliated Hospital of Lanzhou University, comprising 228 CT images of a normal human heart, each with a thickness of 0.5 mm, to reconstruct a 3D model of the
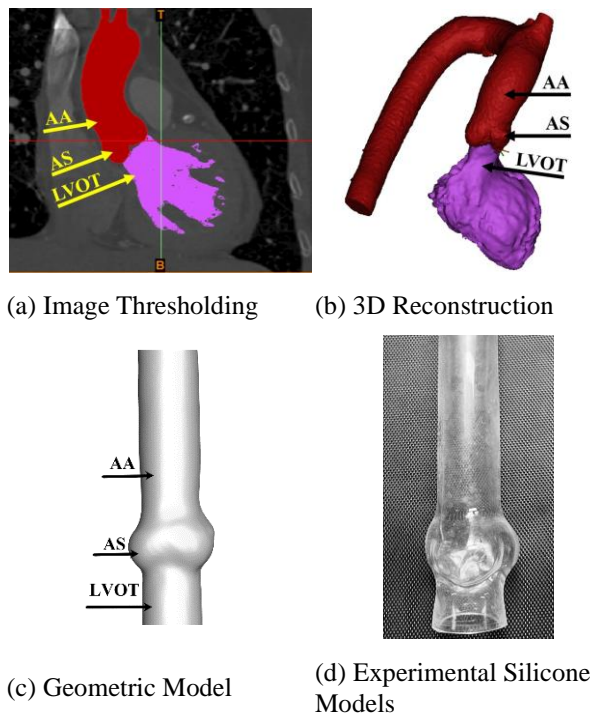
(a) Image Thresholding   (b) 3D Reconstruction

(c) Geometric Model

(d) Experimental Silicone Models

Fig. 1 Overview of aortic root model preparation

(a) Flat-leaflet closure state

(b) Flat-leaflet open state

(c) Schematic diagram of the flat-leaflet structure

(d) Curved-leaflet closure state

(e) Curved-leaflet open state

(f) Schematic diagram of the curved-leaflet structure

Fig. 2 Schematic diagram of the valve photo and the opened and closed structures

aorta. The aorta and LV were segmented using thresholding methods (Fig. 1(a)), followed by the generation of the 3D model (Fig. 1(b)). To refine the ascending aorta, aortic sinuses, LV outflow tract, and LV, software was used to remove excess tissue, smooth surfaces, and Boolean operations were applied to define vessel wall thickness. This process allowed the final construction of the aortic root geometry (Fig. 1(c)), which was then used to 3D-print a silicone aortic model (Fig. 1(d)). The silicone material used in the printing process, designated as PL-X3, had mechanical properties that included a density of 1100 kg/m³, transparency of 98.9%, Shore A hardness of 30, tensile strength of 4.5±0.5 MPa, elongation at break of 350%, tear strength of 12±2 KN/m, and a friction coefficient of 1.32. The refractive index, measured using an Abbe digital refractometer, was 1.413.

For the experiment, we selected the Medtronic Open Pivo™ 505DA24 bileaflet mechanical valve (Medtronic, Minneapolis, USA) as the flat-leaflet aortic valve and the Sorin Bicarbon™ ICV0921 bileaflet mechanical valve (Sorin Biomedica Cardio S.p.A., Saluggia, Italy) as the curved-leaflet aortic valve. These two BMHVs are among the most widely used and clinically applied globally, making the experimental data representative (Qiang et al., 2023a).

Figures 2(a) and 2(d) display the fully closed states of the two valves, while Figs 2(b) and 2(e) show the fully open states. A clear distinction between the two valves lies in the geometry of the leaflets: the flat valve has two semi-lunar planar leaflets, whereas the curved leaflets of the valve are concave, curving toward the annulus. Both designs consist of a polyester sewing ring for fixation, a circular titanium alloy valve ring, and two semicircular occluding leaflets. Detailed specifications of these valves are provided in Table 1. When fully open, the leaflets form
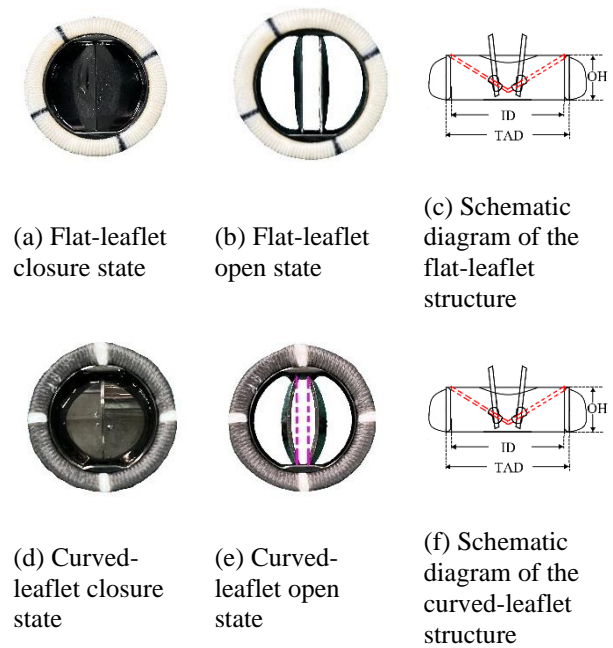
Table 1 Specifications of the Flat- and Curved-Leaflet Bileaflet Mechanical Heart Valves

Aortic Valve Models	Unit	OpenPivotTM Flat-leaflet BMHVs	BicarbonTM curved-leaflet BMHVs
Inside Diameter	mm	22.8	23.3
Ring Diameter	mm	27.5	27.8
Orifice Height	mm	7.9	7.6
Geometric Orifice Area	cm^2	3.84	4.14
Effective Orifice Area	cm^2	3.11	3.06
Maximum Opening Angle	°	82	80
Inside Diameter	mm	22.8	23.3

two lateral orifices and one central orifice (Yoganathan et al., 2004). A hinge pivot mechanism is incorporated into the valve ring, enclosed by the sewing ring. During systole, under a favorable pressure gradient, the leaflets rotate from the fully closed position (as shown by the red dashed line) to the fully open position (black solid line), allowing blood flow. During diastole, under a reverse pressure gradient, the leaflets rotate back, closing the valve and producing a small amount of regurgitation to flush the hinge area (Leo et al., 2002). Figures 2(c) and 2(f) show the leaflet opening and closing mechanisms for both valve types.

2.2 PIV Experiment

PIV is an instantaneous, non-intrusive optical measurement technique that allows full-field visualization of the fluid flow. This technology allows the measurement of instantaneous velocity vectors across the entire field
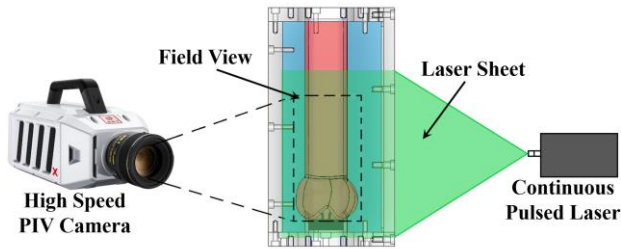

Fig. 3 Schematic diagram of the optical plane

without disturbing the fluid flow, thus enabling visualization of the complete velocity field within the region of interest. It is widely used in experimental studies of aortic valve flow characteristics (Fang et al., 2021). The PIV experimental system primarily consists of a laser light source, high-speed camera image acquisition, computer-based particle image post-processing, and control systems (Pour et al., 2017; Adawy et al., 2018; Qiang et al., 2024).

A 532-nm wavelength, 20 W energy laser (LWPIV-JD-10, Beijing Laizhiwei Optoelectronics Technology Co., China) was used to generate the laser sheet, which was shaped through a cylindrical and spherical lens assembly to illuminate the region of interest uniformly. A high-speed CMOS camera with a resolution of 2560×1920 pixels (Qianyanlang X-150M, Hefei Zhongke Junda Shijie Technology Co., China), fitted with a 50 mm macro fixed-focus lens (SIGMA 50 mm F1.4 DG HSM, Sigma Corporation, Japan), captured the flow field. The camera was positioned at a 90° angle relative to the observation plane, with a measurement field size of 100×100 mm and a pixel size of 5.3 μm. Following multiple tests, a recording rate of 1.5 kHz was chosen, and a total of 60,000 frames were recorded over 50 continuous cardiac cycles. The optical plane of the camera during the experiment is illustrated in Fig. 3.

To match the refractive index of the silicone model and reduce optical distortion in the PIV measurements, a glycerol solution (purity 99%)-distilled water mixture in a 0.56:0.44 volume ratio-was used as the working fluid, with a density of 1147.3 kg/m³, closely approximating that of blood (1060 kg/m³). The dynamic viscosity of the solution was 6.06×10⁻³ Pa·s, 1.18-1.55 times higher than that of blood, which has a reported dynamic viscosity of (4.4±0.5)×10⁻³ Pa·s at 37 °C. The refractive index of the glycerol solution, measured using a refractometer, was 1.4143, closely matching that of the silicone model. Hollow glass beads, with a diameter of 10-14 μm and a density of 1100 kg/m³ (Beijing Betin Measurement Technology Co., China), were used as tracer particles. These particles have a Stokes number far below 1, preventing buoyancy or sedimentation (Xu et al., 2022). The particle size was small enough to accurately follow
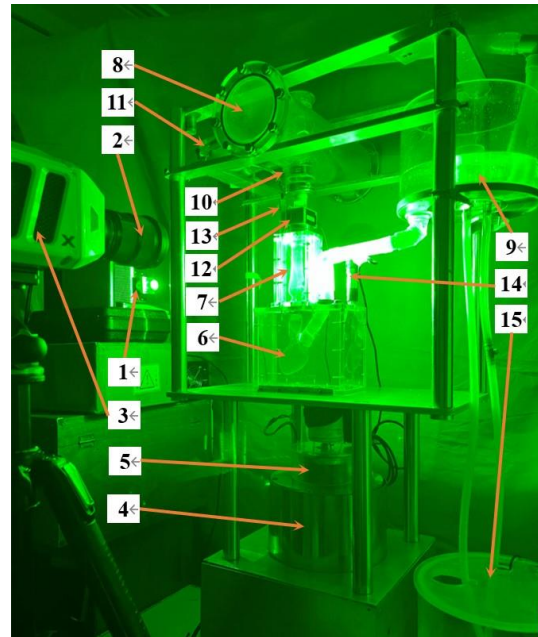

Fig. 4 Overview of the experimental system: 1. Laser, 2. Fixed-focus lens, 3. CMOS high-speed camera, 4-5. Piston and linear motor, 6. Left ventricle, 7. Aortic root, 8. Arterial compliance chamber, 9. Left atrium and venous chambers, 10-11. Peripheral and characteristic damping, 12. Flow transducer, 13-14. Pressure transducer, 15. Reservoir

the fluid motion without disturbing the flow and large enough to reflect sufficient light for capture by the camera. After multiple tests, a seeding density of 30 particles per 36×36 pixels was determined to be optimal for capturing meaningful flow data without introducing excessive noise or under-sampling.

Image preprocessing and flow field analysis were performed using Matlab® PIVlab software. Preprocessing included contrast-limited adaptive histogram equalization filters, high-pass filters, and Wiener noise reduction (Qiu et al., 2022). A multi-pass direct Fourier transform correlation algorithm with window deformation was used to compute instantaneous velocity vectors from particle images, with 50% overlap to meet Nyquist criteria. Two iterations were applied to reduce uncertainty to below 2% (Weinberg et al., 2010). Outlier velocity vectors were removed using a filter based on maximum and minimum acceptable velocity values and replaced with interpolated values from adjacent vectors.

The experimental setup of the pulsatile-flow blood circulation system included a pulsatile pump, an aortic root visualization model, an LV model, arterial and venous chambers, sensors, and an upper computer system, as depicted in Fig. 4. The pulsatile pump, which comprised a linear motor and a piston hydraulic cylinder, served as the driving force for blood circulation throughout the system. The linear motor consisted of a stator connected to a 90-V DC power supply and a rotor fixed to the piston rod via threads and connected to a power amplifier. The upper computer system sent a pulsatile signal through the power amplifier, causing the rotor to drive the piston up and down in the sleeve within a strong magnetic field. The LV

model was submerged in a fluid-filled sealed cavity to simulate LV contraction and relaxation realistically and ensure flow similarity. The bottom of the LV cavity had a through-hole sealed at the top of the piston hydraulic cylinder. The cavity was filled with an incompressible experimental fluid, ensuring that the volume change of the LV directly corresponded to the piston stroke volume. Pressure sensors continuously monitored pressure inside the aortic and LV chambers, and ultrasonic flow sensors recorded downstream flow rates and velocities. A wire displacement sensor tracked the linear motion of the motor, transmitting all data in real time to the data acquisition system for analysis.

A complete cardiac cycle begins when the piston moves downward, simulating LV diastole. As the piston descends, the LV pressure decreases, the mitral valve opens, the aortic valve closes, and the experimental circulating fluid (mimicking blood) flows rapidly from the venous system into the LV, filling it to simulate diastole. LV systole begins when the piston moves upward. In our system, the silicone model of the LV was compressed by increasing the pressure, thereby closing the mitral valve and opening the aortic valve. Circulating blood was pumped from the LV through the aortic valve into the aorta to simulate systole. Circulating blood then flowed from the aorta into the arterial simulation system and back to the venous simulation system through the connecting tubes, completing one cycle of circulation.

Throughout this process, medical pressure sensors were set up to monitor the internal pressures of the aortic and LV chambers, while an ultrasonic flow sensor measured the flow rate and velocity of the circulating blood downstream of the aorta. A draw-wire displacement sensor further monitored the motor displacement data, transmitting the monitored data in real time to a data acquisition card, where it was recorded and saved using the upper computer software. Adjustable arterial compliance chambers, aortic air chambers, and resistance-damping devices were set downstream of the aortic valve to ensure the correct physiological aortic flow and pressure waveforms were generated. The upper computer software subsequently generated appropriate physiological waveforms by adjusting the piston displacement and frequency in real time to simulate the contraction and relaxation of the LV under physiological flow conditions.

The silicone model of the aortic root was placed in a transparent chamber made of acrylic (with light transmittance ≥95%) to simulate the influence of aortic compliance under physiological conditions and ensure the similarity of fluid motion through the aortic valve. This chamber was connected to another small sealed chamber via fine tubes to replicate flow resistance and simulate the elasticity of the aortic system. The ends of the fine tubes were connected to an air-inflated balloon with a valve, allowing adjustment of the air volume injected into the aortic chamber by squeezing the balloon and controlling the valve. This controlled the volume ratio of the sealed gas to the fluid, which was monitored in real-time using pressure sensors, and ultimately controlled the elastic
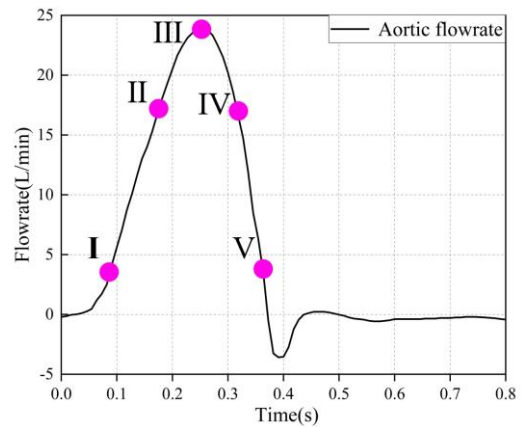

Fig. 5 Flow curves and characteristic moments in the model

performance of the silicone aortic model. This setup ensured that the influence of aortic compliance on blood flow was physiologically achieved. The experimental conditions were subsequently set to mimic a healthy human heart state, with a heart rate of 75 bpm, a stroke volume of 66 mL, an average cardiac output of 5 L/min, an aortic pressure of 70-110 mmHg, an LV pressure of 0-115 mmHg, a left atrial pressure of 8 mmHg, arterial compliance of 2 mL/mmHg, and systemic vascular resistance of 1 mmHg·s/mL. The systole/diastole ratios were set at 45% and 55%. The peak Reynolds number during aortic systole in healthy humans ranges from 5000 to 10000 and is typically approximately 7000 (Qiang et al., 2023a, b). In this study, the peak Reynolds number under healthy conditions was 6543, falling within the normal range.

3. RESULTS AND DISCUSSION

During the complete cardiac cycle, five keyframes were selected to represent the different characteristic phases, as shown in the flow rate curve in Fig. 5. Moment I represents early systole, when the LV starts to contract, causing the aortic valve leaflets to gradually open owing to the induced pressure difference, allowing blood to flow from the LV into the aorta. Moment II represents the acceleration phase of systole, in which the contraction of the LV intensifies, and the aortic valve opens fully. Moment III is the peak systole phase, with the aortic valve leaflets fully open and the blood flow velocity reaching its peak. Moment IV represents the late systole phase, in which the transvalvular flow gradually decreases. Finally, Moment V represents the end-systole phase, marking the end of LV contraction and the initiation of aortic valve closure.

The flow visualization images shown in Fig. 6 present the labeled flow structures, which can be summarized as follows: the left and right sinus recirculation regions (1) and (10) appear as elliptical regions, with the side orifices distinguished as the left-side orifice jet (3), right-side orifice jet (8), central orifice jet (5), and leaflet wake (6), all downstream of the leaflets within the central jet. The shear layers outside of the side orifice jets are termed the left-side orifice shear layer (2) and the right-side orifice
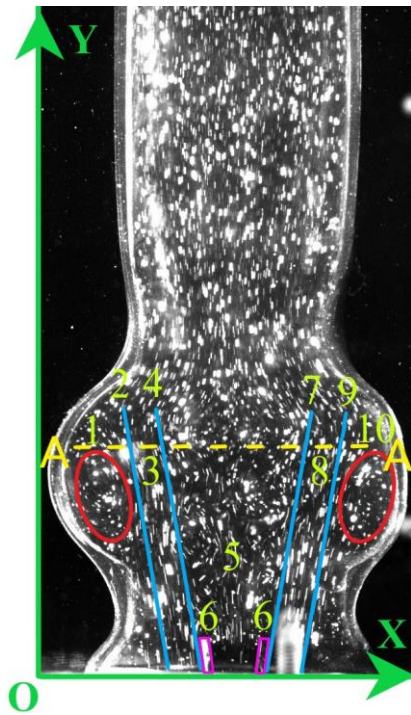
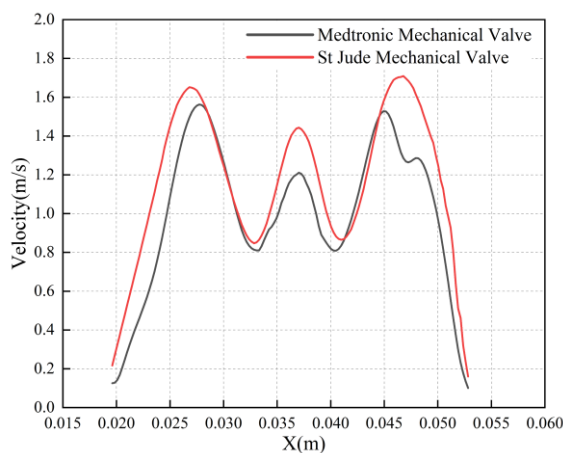**Fig. 6 Visualization image of peak systolic flow**

Fig. 7 Comparative validation of experimental data

shear layer (9), while the shear layers between the side orifice jets and the central jet are termed the left-central jet shear layer (4) and the right-central jet shear layer (7). The blue lines indicate the approximate positions of these shear layers. Leaflets are highlighted in the purple box at the bottom of the image. The coordinate system defines the Y-axis as vertically upward positive and the X-axis as horizontally rightward positive. A characteristic line was selected downstream of the aortic valve (position A-A, Fig. 6) to obtain the velocity profile distribution of the flat valve at this position during peak systole. Referring to the experimental data of the SJM bileaflet flat valve by Hatoum et al. (2022), as shown in Fig. 7, the velocity distribution curves of the two valves were similar in the same position downstream of the aortic valve, aligning with the expected experimental results. They verified the

present experimental reasonableness of the research methodology (Haghighi & Asl 2015; Haghighi et al. 2020).

3.1 Effect of Different Leaflet Shapes on Downstream Velocity Distribution of the Aortic Valve

Figure 8 presents velocity distribution contour maps of the five characteristic moments of blood flow through the BMHV with flat and curved leaflets during a complete cardiac cycle. The upper panel shows the five characteristic moments within the cardiac cycle, and the left panel shows schematic diagrams of the different leaflet valves. At Moment I (early systole), owing to the three-orifice design, the flat and curved bileaflet valves clearly showed jets from the left-sided, right-sided, and central orifices in the contour maps. The jet velocities from the left and right side orifices were nearly identical for both valve types. However, the central orifice jet velocities differed considerably. The flat leaflet valve had a lower central orifice jet velocity, with the side orifices acting as the main outlets, whereas the curved leaflet valve had a larger central orifice jet velocity, exhibiting a three-orifice jet pattern in which the central orifice jet was more dominant than the side orifice jets. At Moment II (acceleration phase of systole), the jets from the side orifices of both valve types formed an inverted V-shape. The flat leaflet valve had slightly higher side-orifice jet velocities and a larger high-speed distribution area than the curved leaflet valve. However, the central orifice jet of the curved leaflet valve was larger than that of the flat leaflet valve, displaying a similar trend in velocity distribution across its side and central orifices.

Both valve types reached peak jet velocities at Moment III (the peak systole phase). Compared to the acceleration phase, the side orifice jets of the flat leaflet valve gradually aligned parallel to the axial direction of the ascending aorta, with only slight deviations at the sinus-tubular junction. Conversely, the side orifice jets of the curved leaflet valve exhibited a larger deviation angle, while the flat leaflet valve had a slightly larger area of high-velocity blood flow distribution. The central orifice jets of both leaflet types were smaller than the side orifice jets at peak systole, with the two side orifices acting as the main outlets. The flat leaflet valve exhibited a more pronounced vortex flow within the sinus than the curved leaflet valve. In Moment IV (late systole phase), the central orifice jets of both valves were substantially smaller than the side orifice jets. The side orifice jets of the flat leaflet valve were primarily situated in the vertical direction relative to the aortic axis, whereas the side orifice jets of the curved leaflet valve tended to move towards the central position at the sinus-tubular junction. This tendency was hypothesized to be due to the curvature of the curved leaflets. At Moment V (end-systole phase), the velocity distribution at the sinus-tubular junction and ascending aorta showed substantial differences between the two valve types. The velocity distribution of the flat leaflet valve was symmetrical, close to the vascular walls on both sides, with lower velocities in the middle region of the ascending aorta. In contrast, the curved leaflet valve had a more uniform velocity distribution in the sinus and ascending aorta regions, with higher velocities in both the sinus sides and the central aorta.
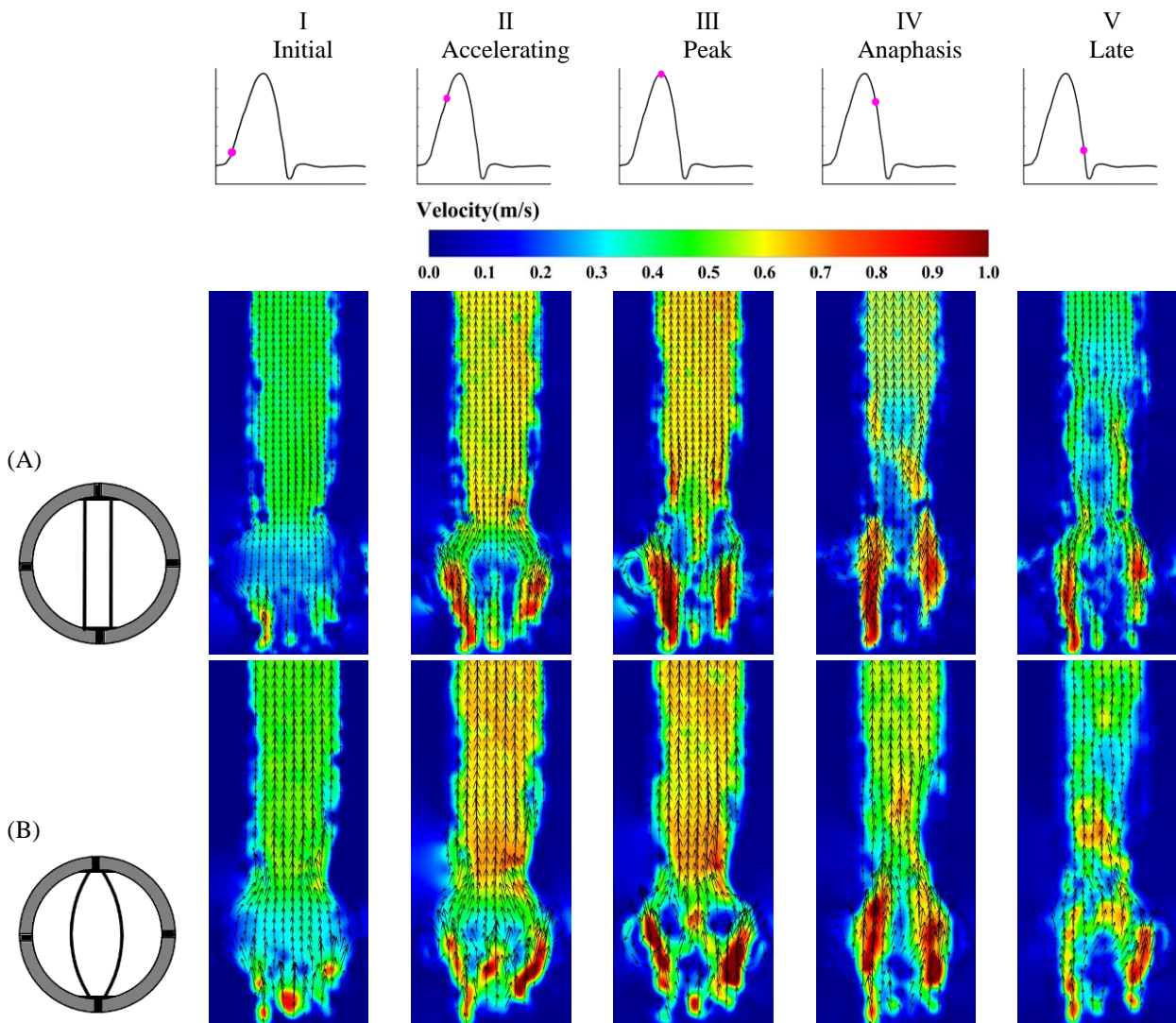
Fig. 8 Exemplar velocity distribution clouds downstream of two different bileaflet mechanical aortic valves. A (I-V) is the velocity distribution cloud of the flat-leaflet valve. B (I-V) is the velocity distribution cloud of the curved-leaflet valve, with a superimposed acceleration vector arrow

The velocities over 10 cycles were time-averaged to gain a more intuitive understanding of the downstream blood flow characteristics of the BMHV with different leaflet shapes. The time-averaged velocity contour maps for a complete cardiac cycle are shown in Fig. 9. For both leaflet structures, the side-orifice jet velocities were substantially higher than the central orifice jet velocities. The key difference was that the high-velocity distribution of the flat leaflet valve extended from the side orifices through the sinus to a large area of the aorta, with the high-speed region narrowly distributed along the vessel wall. The side orifice jets of the curved leaflet valve had a narrow distribution similar to that of the flat leaflet valve near the leaflet tips, with a narrow distribution, while the high-speed region gradually expanded towards the central sinus. In the ascending aorta, the flat leaflet valve showed higher velocities near the vessel wall and much lower velocities near the center, consistent with the observations at the end-systole phase (Moment V). Further, the curved high-speed region of the leaflet valve in the ascending aorta was broadly and nearly uniformly distributed across the entire aorta, indicating that the three-orifice jet
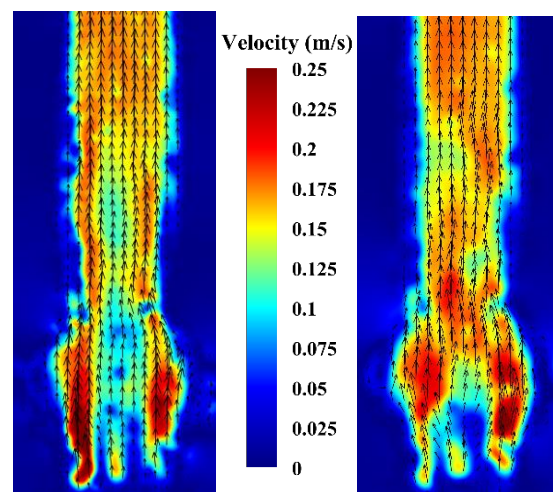

Fig. 9 Cloud plot of the mean velocity distribution downstream of the two different two-leaflet mechanical aortic valves. The mean velocity distribution cloud is shown on the left for the flat-leaflet valve and on the right for the curved-leaflet valve, with superimposed velocity vector arrows
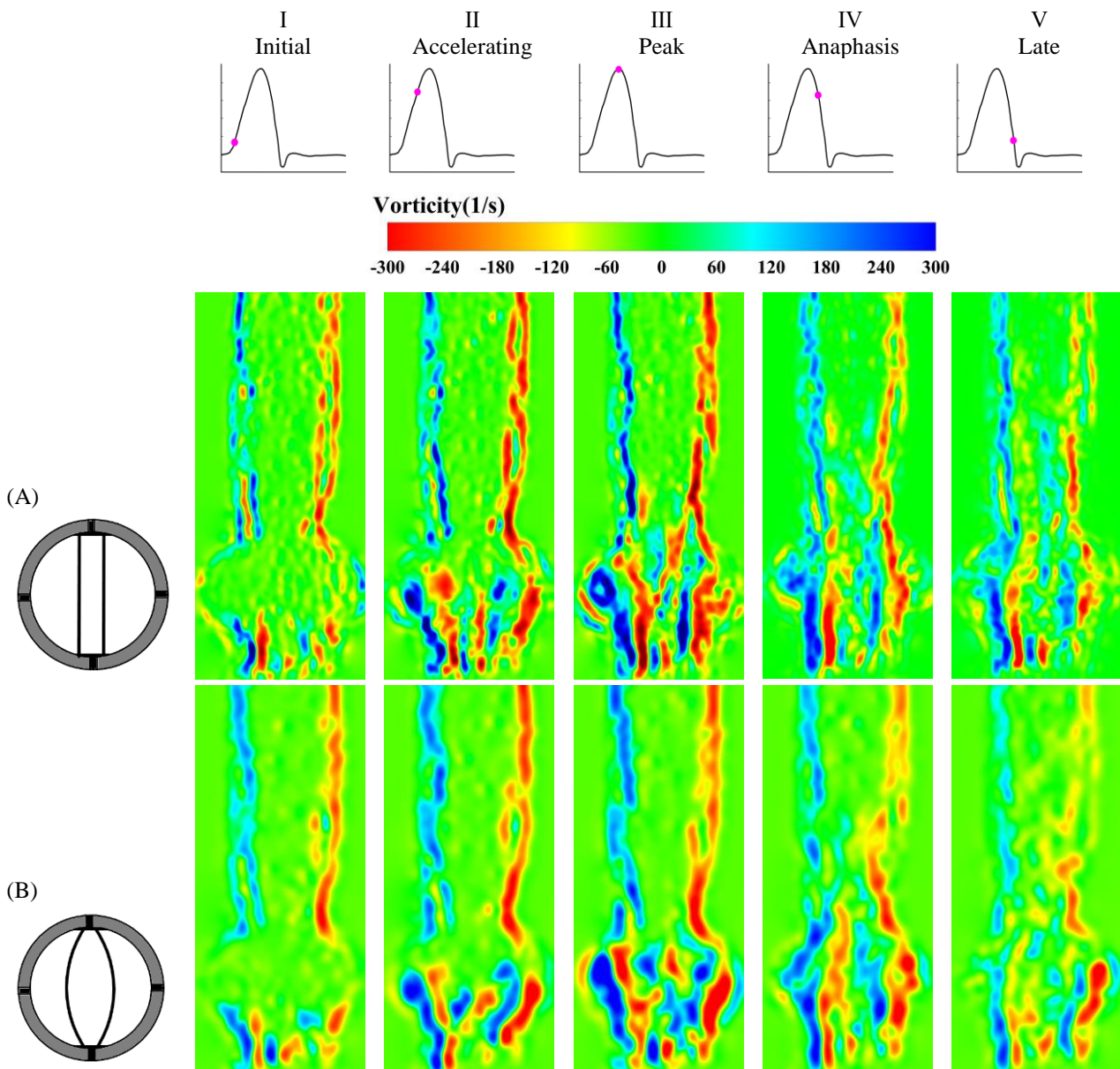
Fig. 10 Vortex evolution cloud maps within the aorta downstream of the two different bileaflet mechanical aortic valves. A (I~V) represents the vortex evolution cloud map of the flat-leaflet valve, and B (I~V) represents the vortex evolution cloud map of the curved-leaflet valve

structure of the curved leaflet had less considerable impact on the downstream flow in the aorta.

3.2 Effect of Different Leaflet Shapes on the Downstream Vortex Evolution of the Aortic Valve

Vorticity can cause abnormal shear stress on the aortic valve, potentially inducing aortic valve disease. The shape of the aortic valve leaflets considerably influences the vortex evolution patterns in the aortic root and sinus. Fig. 10 depicts the vortex evolution patterns downstream of the two valve types at five characteristic moments within the cardiac cycle. The top part of the figure represents the five characteristic moments within the cardiac cycle, while the left side shows the schematic diagrams of the different leaflet valves. In the contour maps, the blue areas indicate counterclockwise vortices, whereas the red areas indicate clockwise vortices. Overall, the vorticity values of the curved leaflets were lower than

those of the flat leaflets. At Moment I (early systole), distinct groups of vortices with opposing directions were observed at the valve outlets, specifically at the exits of the left and right side orifices and the central orifice. The vorticity at the central orifice was slightly higher for the curved leaflet than that for the flat leaflet, possibly because of the higher jet velocity from the central orifice in early systole for the curved leaflet. Continuous vorticity distributions were observed near the walls of the ascending aorta on both sides for both valve types. At Moment II (acceleration phase of systole), blood jetted through the aortic valve, and high-speed vortices shed from the leaflets developed towards the aortic sinuses on both sides. The outer vortices in the side orifice jets were similar for both valve types; however, the inner vortices showed higher vorticity values for the flat leaflet than those for the curved leaflet. The vortices that developed
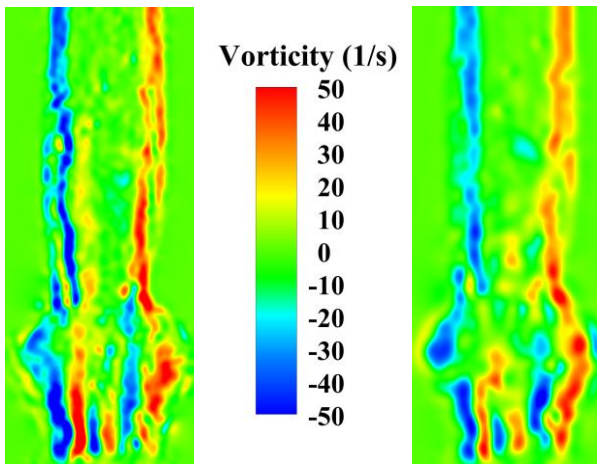
Fig. 11 Cloud plots of the mean vortex distribution downstream of two different two-leaflet mechanical aortic valves. The mean vortex distribution clouds on the left and right show plots for the flat-leaflet and curved-leaflet valves, respectively.

from the central orifice jet exhibited continuous broken vortices for the flat leaflet, whereas the curved leaflet exhibited more structured and regular vortices.

At Moment III (peak systole), both valve types displayed crescent-shaped vortices on the walls of the aortic sinuses resulting from the high-speed rotation of the blood within the sinuses. The inner vortices near the side orifice jets for the flat leaflet broke up and dissipated upon reaching the sinus-tubular junction, whereas the curved leaflet maintained a more intact vortex structure upon impact with the sinus-tubular wall. The vortex formed by the central orifice jet of the curved leaflet moved downstream in the ascending aorta in a complete form. At Moment IV (late systole), the elliptical vortices within the aortic sinuses were gradually carried towards the ascending aorta by subsequent side orifice jets, leading to the fragmentation of the vortices within the sinuses. Conversely, for the flat leaflet, the vortices within the sinuses were disrupted and broken, and the opposite inner vortices gradually dissipated as they flowed downstream along the aortic wall. In contrast, the curved leaflet formed new vortices upon impact at the sinus-tubular junction wall, merging and colliding with the vortices in the opposite direction from the side orifices and central orifice at the sinus exit. At Moment V (end-systole), the overall vorticity values were higher for the flat leaflets than those for the curved leaflets. The flat leaflet showed vortex development near the aortic walls in both the sinuses and ascending aorta, whereas the curved leaflet exhibited more chaotic and disordered vortices throughout the entire region, with fragmented vortices resulting from the merging and collision of the three groups of vortices.

The time-averaged vorticity over 10 cycles is shown in the average vorticity contour maps for a complete cardiac cycle in Fig. 11. The overall vorticity of the flat-leaflet aortic valve was greater than that of the curved-leaflet aortic valve. Three distinct groups of vortices with different directions could be observed at the valve exits for both valve types. The vortices near the sides of the side

orifices of the curved leaflet deflected considerably towards the central axis after shedding from the leaflet tips and gradually dissipated upon entering the ascending aorta. In contrast, vortices from the side orifices of the flat leaflet developed downstream along the aortic walls before gradually dissipating into the deeper regions of the ascending aorta. Overall, the vorticity and distribution areas of the curved leaflets were smaller than those of the flat leaflets.

3.3 Effect of Different Leaflet Shapes on the Downstream Viscous Shear Stress Distribution of the Aortic Valve

VSS characterizes the shear action between adjacent fluid layers and represents the physical shear stress experienced by blood cells. This stress highlights the intensity of the spatial velocity gradients and reflects the physical forces exerted by the fluid on suspended blood cells, which are closely related to valve thrombosis, platelet activation, and hemolysis (Gunning et al., 2014). This is defined in Eq. (1).

$$VSS = \mu(\frac{\partial u}{\partial y} + \frac{\partial v}{\partial x}) \tag{1}$$

where μ is the dynamic viscosity of the working fluid.

Figure 12 illustrates the shear stress distribution contour maps at five characteristic moments within a complete cardiac cycle for both the flat and curved BMHVs. The top section of the figure represents the five characteristic moments within the cardiac cycle, while the left side shows the schematic diagrams of the different leaflet valves. At Moment I (early systole), blood jetted out through the left- and right-sided orifices and the central orifice, forming six main shear layers. The left- and right-side orifice jets further created four symmetric shear layers owing to the velocity gradient differences between the near-wall regions of the aortic sinuses and the outer surface areas of the leaflets. The central orifice jet further formed two shear layers owing to the velocity differences between the jet and the inner surface areas of the leaflets. The shear layers of the left and right side orifices were similar for both valves. However, the central orifice shear layer value was slightly higher for the curved leaflet than that for the flat leaflet. At Moment II (acceleration phase of systole), the shear layer formed by the central orifice jet of the curved leaflet was smaller and primarily concentrated in the inner region of the leaflet tip, whereas the flat leaflet exhibited a longer region of shear layer formation.

At Moment III (peak systole), the shear layer values for the left and right side orifices of both valves were high, with maximum shear stresses of 1.93 N/m^2 and -1.88 N/m^2 for the flat leaflet, respectively. The curved leaflet had slightly lower maximum shear stresses of 1.85 N/m^2 and -1.87 N/m^2, respectively. Ge et al. (2005) found that a higher instantaneous VSS led to increased turbulence and a higher incidence of blood damage in the downstream field. They further showed that instantaneous VSS exceeding the critical value of 2 N/m^2 may activate platelets. Both valves in our model exhibited maximum
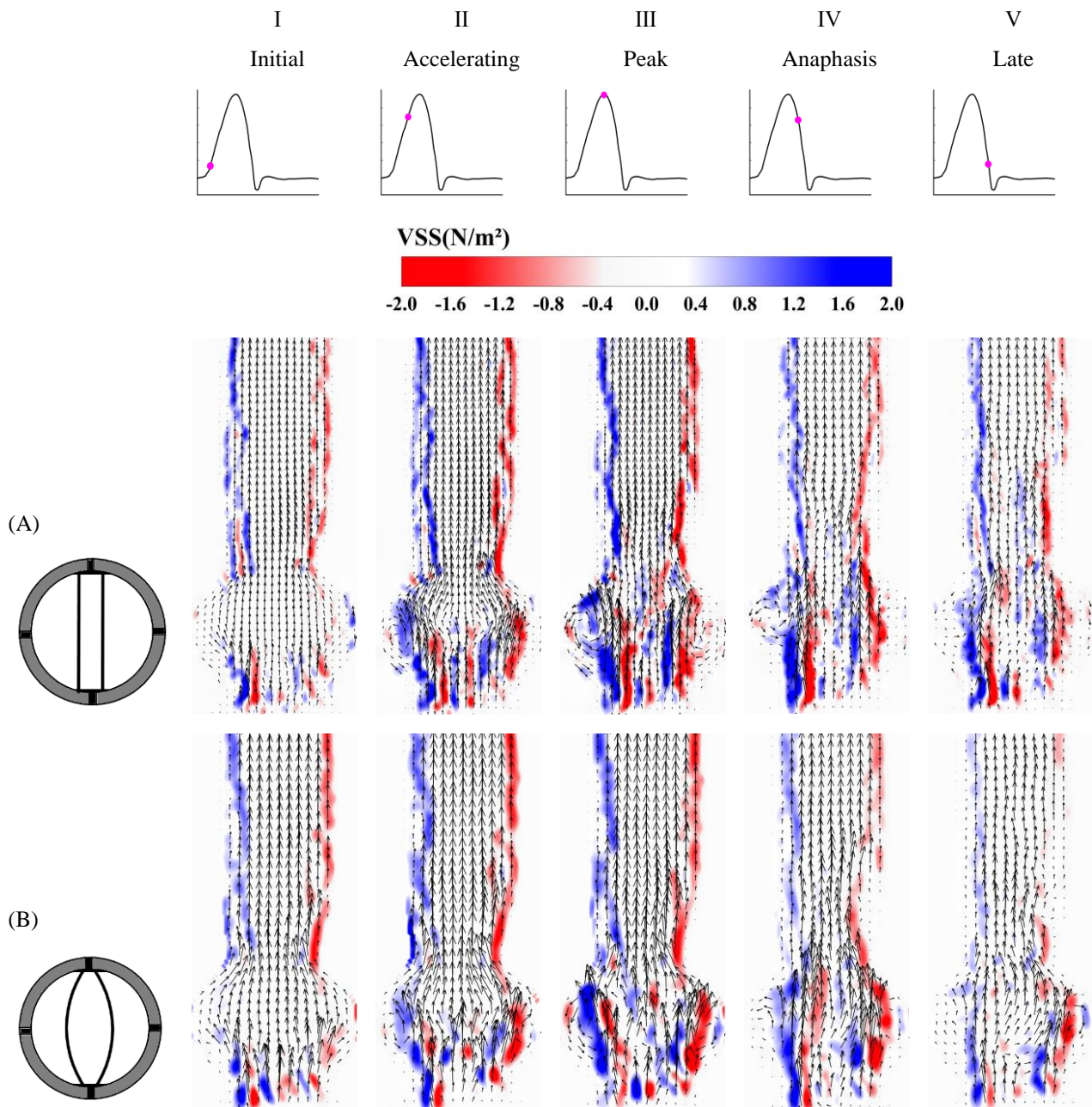
Fig. 12 Cloud plots of the viscous shear stress distribution downstream of two different bileaflet mechanical aortic valves. A (I~V) presents the viscous shear stress distribution cloud plot of the flat-leaflet valve. B (I~V) presents the viscous shear stress distribution cloud plot of the curved-leaflet valve with superimposed acceleration vector arrows

VSS values below the damage threshold proposed by Ge et al. (2005). Specifically, the flat leaflet exhibited higher shear stress values on the ascending aortic wall at peak systole and a larger distribution area at the aortic sinus exit than the curved leaflet. At Moment IV (late systole), owing to the influence of the curved leaflet, the velocity gradient differences between the outflowing blood from the leaflet tips and the recirculating blood in the sinuses resulted in larger shear layers at the sinus-tubular junction for the curved leaflet than for the flat leaflet. At this Moment, the viscous shear layers formed by the central orifice jet gradually disappeared. At Moment V (end-systole), apart from the small shear layers formed by the

side orifice jets, the majority of the shear layers disappeared as the blood jets ceased.

3.4 Effect of Different Leaflet Shapes on the Downstream Reynolds Shear Stress Distribution of the Aortic Valve

RSS is a mathematical artifact arising from the Reynolds decomposition of the Navier-Stokes equation. It is a statistical measure of the shear stress of the velocity field between fluid flow layers caused by temporal variations in the velocity field. RSS, representative of turbulent shear stress, is closely related to hemocyte damage and is used to predict potential hemolysis zones (Ge et al., 2005; Gunning et al., 2014). The Reynolds
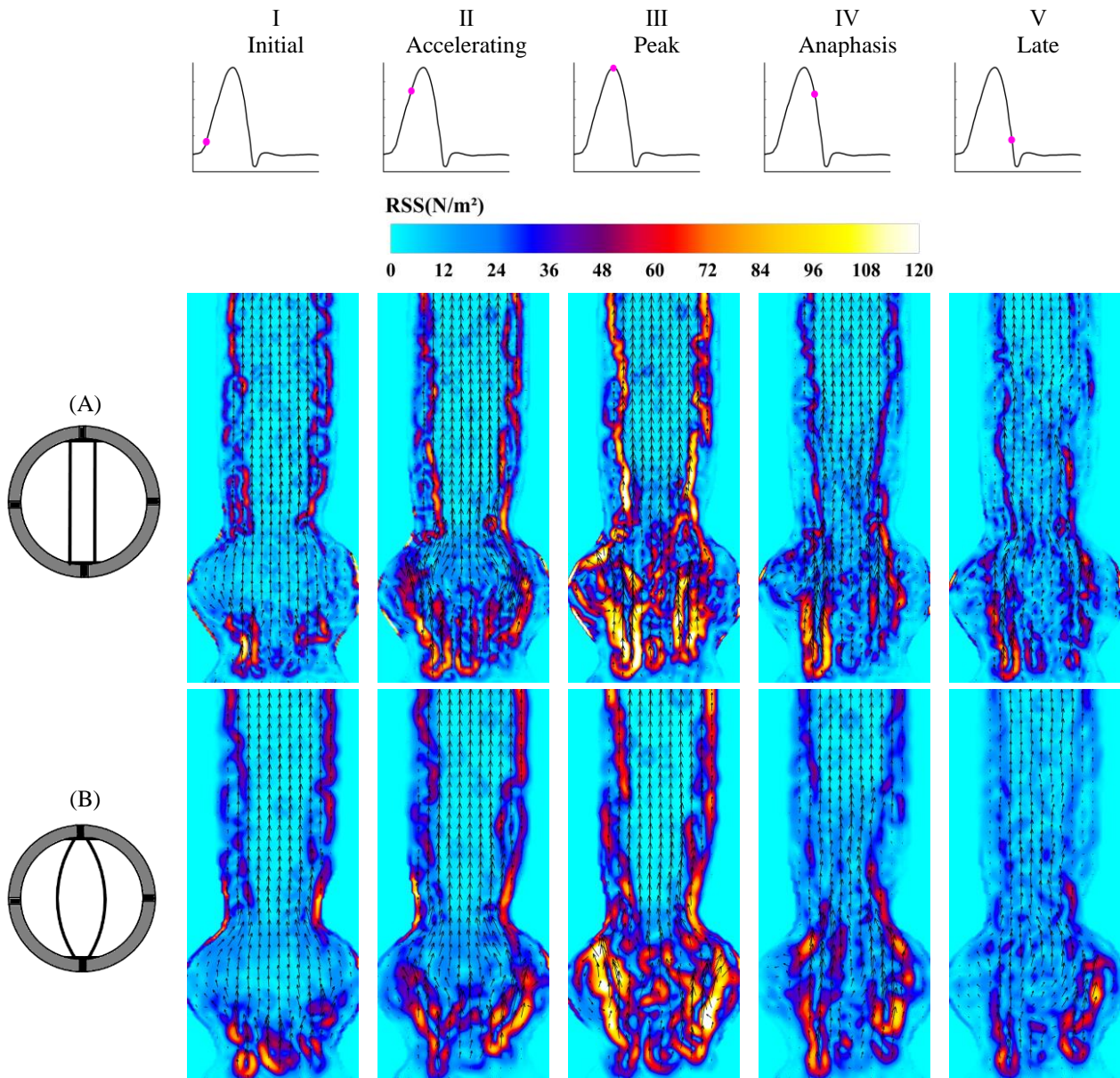
Fig. 13 Reynolds shear stress distribution clouds downstream of two different bileaflet mechanical aortic valves. A (I~V) prevents the Reynolds shear stress distribution cloud of the flat-leaflet valve, and B (I~V) presents the Reynolds shear stress distribution cloud of the curved-leaflet valve with superimposed acceleration vector arrows

decomposition method can decompose velocity into time-averaged velocity $\overline{u}$ and instantaneous velocity fluctuations u'. In this study, the time-averaged velocity at each Moment in the cardiac cycle was obtained by averaging the velocity fields over 50 cycles, while instantaneous velocity fluctuations were determined by subtracting the time-averaged velocity from the instantaneous velocity. The RSS is defined by Eqs/ (2)-(4).

$$u' = u - \overline{u} \tag{2}$$

$$v' = v - \overline{v} \tag{3}$$

$$RSS = \rho\sqrt{\left(\frac{\overline{u'u'} - \overline{v'v'}}{2}\right)^2 + \left(\overline{u'v'}\right)^2} \tag{4}$$

where ρ is the density of the simulated blood fluid, u' is the instantaneous velocity fluctuation in the x direction,

v' is the instantaneous velocity fluctuation in the y direction, $\overline{u}$ is the time-averaged velocity in the x direction, and $\overline{v}$ is the time-averaged velocity in the y direction.

Figure 13 shows the shear stress distribution contour maps at five characteristic moments within a complete cardiac cycle for both the flat and curved BMHVs. The top section of the figure represents the five characteristic moments within the cardiac cycle, while the left side shows the schematic diagrams of the different leaflet valves. During Moment I (early systole), the leaflets opened, and blood jetted out through the left-sided, right-sided, and central orifices owing to the asymmetric pressure on both sides of the leaflets. Both the flat and curved leaflets exhibited considerable turbulence in the side orifice jets, with the central orifice jet of the curved leaflet showing a more unstable flow than that of the flat

leaflet. This was also inferred from the previous velocity distribution analysis, in which the central orifice jet of the curved leaflet had a higher velocity and flow rate than those of the flat leaflet. In Moment II (acceleration phase of systole), the central orifice exit of the flat leaflet showed a considerable RSS distribution owing to the leaflet shape, whereas the curved leaflet exhibited less turbulence in the inner side jet. The side orifice jets of both the leaflets exhibited similar turbulence levels. In Moment III (peak systole), the symmetric transvalvular flow reached its maximum speed. High-speed transvalvular flow and relatively slow flow in the ascending aorta created shear layers near the aortic wall. Owing to large velocity fluctuations, regions with high RSS were formed. The overall RSS of the flat leaflets was higher than that of the curved leaflets, with maximum RSS values of 152 and 118 N/m². Dasi et al. (2009) have previously suggested that RSS values exceeding 100 Pa could cause considerable blood cell damage and hemolysis. Although substantial turbulence still existed, hindering physiological blood flow, the curved leaflet design reduced turbulence and blood flow fluctuations compared to the flat leaflet design. The RSS layers that formed on the inner sides of the side orifices of the flat leaflets were noticeably larger than those of the curved leaflets. Additionally, the flat leaflet exhibited higher turbulence levels in the middle region of the aortic sinuses, indicating stronger turbulence in this region. In Moment IV (late systole) and Moment V (end-systole), both leaflets showed slightly stronger shear layers at the left and right side orifices than the other regions. The overall RSS distribution for both valves diminished with decreased blood jetting velocity and flow rate. Akutsu & Fukuda (2005), Akutsu & Saito (2006), Akutsu, et al. (2008), and Akutsu & Matsumoto (2010) studied a variety of mechanical valves under pulsatile flow conditions and showed that straight-sided valves produce considerably higher turbulent stresses than curved valves. Our findings align with this and further confirm that straight-sided flap leaflet design leads to higher turbulence.

The ability of the BMHVs to minimize blood damage during surgery is termed "hemocompatibility." Potential types of blood damage include hemolysis, platelet activation, coagulation changes, thrombosis, leukocyte function reduction, and von Willebrand factor (vWf) damage (Leverett et al., 1972). Hemolysis refers to the damage to red blood cells, resulting in the release of hemoglobin into the plasma. Excessive mechanical shear stress on red blood cells can tear the cell membrane or form holes, resulting in the leakage of hemoglobin into the plasma. Shear stress exceeding 100 Pa can directly cause hemolysis (Dasi et al., 2009). Platelets are small, biologically active cytoplasmic fragments in the blood that play crucial roles in physiological hemostasis and pathological thrombosis. Platelets can be activated by abnormal shear stress acting on the vWf attached to platelet GPIbα receptors or through the dissolution of the activators stored in platelets and red blood cells. According to Fraser et al. (2012), the shear stress threshold for platelet activation in the aorta is 50 Pa. vWf, a high-molecular-weight polymer secreted by endothelial cells, is
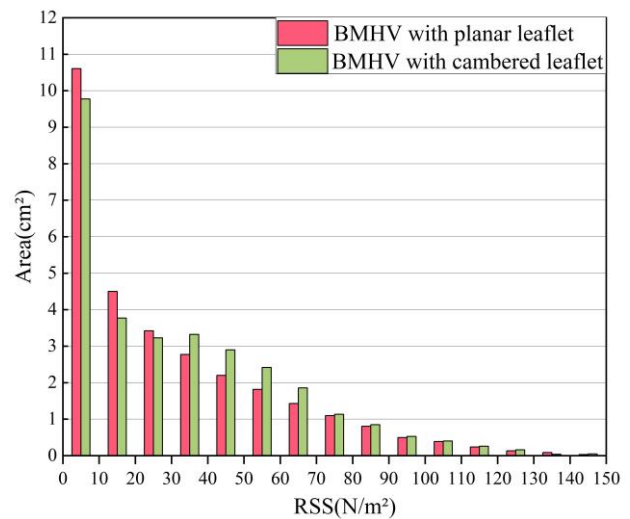

Fig. 14 Area distribution of the Reynolds shear stress in the flow field downstream of the aortic valve
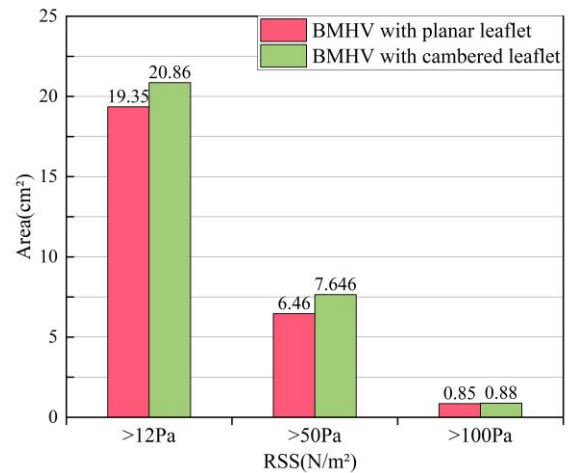

Fig. 15 Area distribution of the flow field above a specific Reynolds shear stress threshold

crucial for platelet deposition and aggregation, and plays a critical role in normal hemostasis. Shear stress in the circulatory system can alter the composition of the vWf, making it more susceptible to proteolysis. Colantuoni et al. (1977) found that shear stress exceeding 12 Pa could rapidly cause vWf fragmentation and reduction. In our study, the shear stress thresholds for hemolysis, platelet activation, and vWf reduction were defined as 100, 50, and 12 Pa, respectively.

The areas corresponding to the different levels of RSS downstream of the flat and curved BMHVs are shown in Fig. 14. In the 0-30 Pa range, the area with the RSS for the flat BMHVs was slightly larger than that for the curved BMHVs. Further, in the 30-70 Pa range, the area with the RSS for the curved BMHV was considerably larger than that for the flat BMHV. In the 80-150 Pa range, the area with the RSS for the curved BMHV was slightly larger, but the difference was not particularly substantial.

The areas corresponding to the shear stress thresholds for blood damage in the flat and curved BMHVs are presented in Fig. 15. For the 12 Pa vWf damage threshold and 50 Pa platelet activation threshold, the area of the curved BMHV was slightly larger than that of the flat

BMHV. For the 100 Pa hemolysis threshold, there was no substantial difference between the two. Thus, the risk of vWf damage and platelet activation in the curved BMHV was slightly higher than that in the flat BMHV; however, the overall impact was not substantial.

4. LIMITATIONS AND FUTURE WORK

First, this study used a silicone model to simulate the aortic root. However, the elastic modulus of silicone differed from that of human blood vessels, which affected the interaction between blood flow and the vessel wall. Consequently, the experimental results were not entirely consistent with physiological conditions. Additionally, the surface microstructure of the silicone material differed from that of the human vessel wall, affecting flow resistance and shear stress. These simplifications can provide some experimental basis, but materials closer to physiological conditions should be considered in future studies. Second, our study ignored the coronary arteries and aortic arch in the aortic sinus lumen, which affect the flow field and leaflet motion. Future model design should consider these anatomical structures to closely approximate the natural physiologic environment. Third, blood flow in the aortic root is inherently three-dimensional; however, we used the 2D-2C PIV technique to obtain the two-dimensional flow field downstream of the aorta. Two-dimensional planar PIV measurements only partially capture the three-dimensional information of the flow field. Future studies should use 4D-MRI or Tomo-PIV techniques combined with CFD numerical simulation to obtain more comprehensive flow field data, thus providing more reliable data support for valve optimization design.

5. CONCLUSION

This study investigated the blood flow field characteristics downstream of BMHVs with flat and curved leaflets under physiological pulsatile flow conditions using 3D-printed silicone models of real aortic roots derived from medical CT images on an in vitro blood circulation test bench. Employing PIV technology, we analyzed the impact of leaflet shape on velocity distribution, vortex evolution, VSS, and RSS in the aortic root, aortic sinus, and ascending aorta. Our findings provide experimental data to facilitate preoperative valve selection, improve our understanding of the relationship between postoperative complications and fluid dynamics, and refine simulation calculations. Comparison with other related studies, such as Akutsu & Fukuda (2005), Akutsu & Saito (2006), Akutsu, et al. (2008), and Akutsu & Matsumoto (2010), showed that different valve leaflet shapes have similar effects on the flow field characteristics downstream of the valve. Our study further validates these results, especially regarding turbulence and shear stress distribution, with the following main conclusions:

(1) Flow Distribution and Wall Impact: When blood flowed through the side and central orifices of the valve, the outflow from the central orifice of the curved leaflet was greater than that from the flat leaflet. This design reduced the average velocity in the side orifices from 0.28 m/s (flat leaflet) to 0.231 m/s (curved leaflet). The structural design of the curved leaflet directed the outflow towards the center of the vessel, thereby reducing the impact on the wall at the junction of the aortic sinus and aorta. This can help protect the endothelial cells on the vessel wall and prevent thromboembolism. The larger outflow area at the aortic sinus with the curved leaflet design prevents slow or stagnant blood flow in the central region of the sinus, thus reducing the concentration of clotting factors and thrombin necessary for clot formation and ultimately lowering the risk of thrombosis. Curved leaflets are more suitable for older patients because of their ability to minimize wall impingement of blood on the aortic sinus-tubular junction. Older patients often have weaker vessel walls, making them more susceptible to vascular injury and thromboembolism after aortic valve replacement. Preoperative planning may consider prioritizing the curved leaflet design to reduce the incidence of vascular endothelial cell injury and related complications. Further, curved valves have a larger overflow area at the exit of the aortic sinus cavity, allowing them to better maintain blood flow at lower blood velocities. They are a superior choice for patients with cardiac ejection insufficiency and can be an essential consideration in preoperative planning for valve selection, thereby improving surgical outcomes and patient recovery after surgery.

(2) Vortex Formation and Platelet Interaction: The three orifices of the aortic valve create three sets of counter-rotating vortices. The side orifice jets formed vortices that flowed into the left and right sinuses, thereby effectively avoiding blood stasis. The curvature of the curved leaflets caused high-intensity vortex collisions and breakdowns, leading to a lower vorticity near the ascending aortic wall than the flat leaflet. This reduced the likelihood of platelets adhering to the endothelium, thus decreasing the risk of thrombosis. Choosing a curved leaflet valve with an appropriate curvature for aortic valve replacement could thus be clinically advantageous compared to a flat leaflet valve.

(3) Shear Stress and Blood Cell Damage: During peak systole, the flat leaflet valve showed higher VSS on the ascending aorta wall, with maximum values of 1.93 N/m^2 and 1.87 N/m^2 for the flat and curved leaflets, respectively. Prolonged exposure to mechanical stress can increase the permeability of red blood cells, resulting in fragmentation. The maximum RSS of the flat leaflet was higher (152 N/m^2) than that of the curved leaflet (118 N/m^2). Under turbulent conditions, the curved leaflet demonstrated better performance in reducing shear stress-induced damage to blood cells. The structural design of the curved leaflet mitigated the shear stress on blood cells, reducing platelet activation and the risk of postoperative thromboembolism-related complications.

(4) Shear Stress Distribution: In low RSS regions, the area covered by the curved leaflet valve was substantially larger than that covered by the flat leaflet valve. Conversely, in the higher shear stress region (80-150 Pa), no considerable difference was observed between the two. For blood damage shear stress thresholds, using a vWf damage threshold of 12 Pa and platelet activation

threshold of 50 Pa, the area covered by the curved leaflet valve was found to be slightly larger than that of the flat leaflet valve. However, at a hemolysis damage threshold of 100 Pa, there was no considerable difference between the two.

The structural design of curved leaflets effectively reduced postoperative thromboembolism compared to straight leaflet aortic BMHVs. This study can provide experimental data to support the selection of preoperative valve parameters and optimization of valve hemodynamic performance. The flow field characteristics of curved valve leaflets with various curvature profiles should be further investigated in future studies to determine the optimal valve structural design.

6. ETHICAL APPROVAL

The use of CT images during the study was communicated to the hospital and volunteers, and authorization and consent were obtained. All image data were handled by guidelines for patient confidentiality and data protection. The relevant ethics committee reviewed and approved the study to ensure compliance with ethical standards in medical research.

ACKNOWLEDGEMENTS

CONFLICT OF INTEREST

The authors have no relevant financial or nonfinancial interests to disclose.

AUTHORS CONTRIBUTION

Yan Qiang: conceptualization; data curation; formal analysis; funding acquisition; methodology; project administration; resources; supervision; validation; visualization; writing-original draft; and writing-review and editing. **Tianci Duan**: conceptualization; data curation; formal analysis ; methodology; resources; validation; and visualization. **Minzu Zhang**: conceptualization; investigation; resources; validation; and writing-review and editing. **Liang Qi**: conceptualization; investigation; methodology; and validation. **Liejiang Wei**: conceptualization; formal analysis; investigation; supervision; and validation.

REFERENCES

Adawy, M. E., Heikal, M., Aziz, A. R., Munir, S., Siddiqui, M. I., & Mobility, E. (2018). Effect of boost pressure on the in-cylinder tumble- motion of GDI engine under steady-state conditions using Stereoscopic-PIV. *Journal of Applied Fluid Mechanics*, *11*(3), 733-742. https://doi.org/10.18869/ACADPUB.JAFM.73.246.2

8506.

Akutsu, T., & Fukuda, T. (2005). Time-resolved particle image velocimetry and laser doppler anemometry study of the turbulent flow field of bileaflet mechanical mitral prostheses. *Journal of Artificial Organs*, *8*(3), 171-183. https://doi.org/10.1007/s10047-005-0298-8.

Akutsu, T., & Matsumoto, A. (2010). Influence of three mechanical bileaflet prosthetic valve designs on the three-dimensional flow field inside a simulated aorta. *Journal of Artificial Organs*, (4), 207-217. https://doi.org/10.1007/s10047-010-0519-7.

Akutsu, T., & Saito, J. (2006). Dynamic particle image velocimetry flow analysis of the flow field immediately downstream of bileaflet mechanical mitral prostheses. *Journal of Artificial Organs*, *9*(3), 165-178. https://doi.org/10.1007/s10047-006-0340-5.

Akutsu, T., Saito, J., Imai, R., Suzuki, T. X., & Cao, X. D. (2008). Dynamic particle image velocimetry study of the aortic flow field of contemporary mechanical bileaflet prostheses. *Journal of Artificial Organs*, *11*(2), 75-90. https://doi.org/10.1007/s10047-008-0410-y.

Black, M. M., & Drury, P. J. (1994). Mechanical and other Problems of Artificial Valves. *Current Topics in Pathology Ergebnisse der Pathologie*, *86*, 127-159. https://doi.org/10.1007/978-3-642-76846-0_4.

Chandran, K. B., Khalighi, B., & Chen, C. J. (1985). Experimental study of physiological pulsatile flow past valve prostheses in a model of human aorta-I. Caged ball valves. *Journal of Biomechanics*, *10*(18), 763-765. https://doi.org/10.1016/0021-9290(85)90051-X.

Chew, Y. T., Low, H. T., Lee, C. N., & Kwa, S. S. (1993). Laser anemometry measurements of steady flow past aortic valve prostheses. *Journal of Biomechanical Engineering*, *115*(3), 290-298. https://doi.org/10.1115/1.2895489.

Colantuoni, G., Heliums, J. D., Moake, J. L., & Alfrey, C. P. (1977). The response of human platelets to shear stress at short exposure times. *ASAIO Journal*, *23*(1), 626-630. https://doi.org/10.1097/00002480-197700230-00169.

Dasi, L. P., Simon, H. A., Sucosky, P., Sucosky, P., & Yoganathan, A. (2009). Fluid mechanics of artificial heart valves. *Clinical and Experimental Pharmacology & Physiology*, *36*(2), 225-237. https://doi.org/10.1111/j.1440-1681.2008.05099.x.

Fang, Y. J., Zhang, M., Sun, X. P., Zhang, J. F., & Qu, Y. F. (2021). Study on internal flow characteristics of non-newtonian fluids in mechanical stirred tank. *Journal of Mechanical Engineering*, *57*(20), 244-253. https://doi.org/10.3901/jme.2021.20.244.

Fraser, K. H., Zhang, T., Taskin, M. E., Griffith, B. P., & Wu, Z. J. (2012). A quantitative comparison of mechanical blood damage parameters in rotary ventricular assist devices: shear stress, exposure time

and hemolysis index. *Journal of Biomechanical Engineering*, *134*(8), 081002. https://doi.org/10.1115/1.4007092.

Garg, P., Markl, M., Sathananthan, J., Sellers, S. L., Meduri, C.,& Cavalcante, J. (2023). Restoration of flow in the aorta: a novel therapeutic target in aortic valve intervention. *Nature Reviews Cardiology*, *21*(4), 264-273. https://doi.org/10.1038/s41569-023-00943-6.

Ge, L., Leo, H., Sotiropoulos, F., & Yoganathan, A. P. (2005). Flow in a mechanical bileaflet heart valve at laminar and near-peak systole flow rates: CFD simulations and experiments. *Journal of Biomechanical Engineering*, *127*(5), 782-797. https://doi.org/10.1115/1.1993665.

Grigioni, M., Daniele, C., D'Avenio, G., & Barbaro, V. (2001). The influence of the leaflets' curvature on the flow field in two bileaflet prosthetic heart valves. *Journal of Biomechanics*, *34*(5), 613-621. https://doi.org/10.1016/S0021-9290(00)00240-2.

Gunning, P. S., Saikrishnan, N., McNamara, L. M., & Yoganathan, A. P. (2014). An in vitro evaluation of the impact of eccentric deployment on transcatheter aortic valve hemodynamics. *Annals of Biomedical Engineering*, *42*(6), 1195-1206. https://doi.org/10.1007/s10439-014-1008-6.

Haghighi A. R., & Asl, M. S. (2015). Mathematical modeling of micropolar fluid flow through an overlapping arterial stenosis. *International Journal of Biomathematics*, *04*(08), 1550056. https://doi.org/10.1142/S1793524515500564.

Haghighi, A. R., Aliashrafi, N., & Asl, M. S. (2020). An implicit approach to the micropolar fluid model of blood flow under the effect of body acceleration. *Mathematical Sciences*, *14*(3), 269-277. https://doi.org/10.1007/s40096-020-00340-x.

Hatoum, H., Ahn, S., Lilly, S. M., Maureira, P., Crestanello, J. A., Thourani, V. H., & Dasi, L. P. (2022). Flow dynamics of surgical and transcatheter aortic valves: Past to present. *JTCVS Open*, *9*, 43-56. https://doi.org/10.1016/j.xjon.2022.01.017.

Horstkotte, D., Haerten, K. J., Herzer, J. A., Seipel, L ., Bircks, W., & Loogen, F. (1981). Preliminary clinical and hemodynamic results after mitral valve replacement using St. Jude Medical prostheses in comparison with the Björk-Shiley valve. *The Thoracic and Cardiovascular Surgeon*, *29*(2), 93-99. https://doi.org/10.1055/s-2007-1023451.

Kawahito, K., & Nosé, Y. (2008). Hemolysis in different centrifugal pumps. *Artificial Organs*, *21*(4), 323-326. https://doi.org/10.1111/j.1525-1594.1997.tb00369.x.

Knoch, M., Reul, H., Kröger, R., & Rau, G. (1988). Model studies at mechanical aortic heart valve prostheses-Part I: Steady-state flow fields and pressure loss coefficients. *Journal of Biomechanical Engineering*, *110*(4), 334-343. https://doi.org/10.1115/1.3108450.

Leo, H. L., He, Z., Ellis, J. T., & Yoganathan, A. P. (2002). Microflow fields in the hinge region of the CarboMedics bileaflet mechanical heart valve design. *Journal of Thoracic and Cardiovascular Surgery*, *124*(3), 561-574. https://doi.org/10.1067/mtc.2002.125206.

Leverett, L. B., Hellums, J. D., Alfrey, C. P., & Lynch, E. C. (1972). Red blood cell damage by shear stress. *Biophysical Journal*, *12*(3), 257-273. https://doi.org/10.1016/S0006-3495(72)86085-5.

Linde, T., Hamilton, K. F., Navalon, E. C., Schmitz-Rode, T., & Steinseifer, U. (2012). Aortic root compliance influences hemolysis in mechanical heart valve prostheses: an in-vitro study. *The International Journal of Artificial Organs*, *35*(7), 495-502. https://doi.org/10.5301/ijao.5000108.

Liu, Z. M., Xue, H. B., Yang, G., Pang, Y., Fang, Y. C., Li, M. Q., Qi, Y. P., & Shi, Y. (2020). PIV experimental study on the hemodynamics of aortic valve under varied tilted angles. *Chinese Journal of Theoretical and Applied Mechanics*, *52*(6), 1811-1821. https://doi.org/10.6052/0459-1879-20-229.

Liu, Z. M., Yang, G., Pang, Y., Zhong, X. X., Li, M. Q., Xue, H. B., Qi, Y. P., & Shi, Y. (2019). Experimental study on hemodynamics of aortic valve under varied cardiac output using PIV. *Chinese Journal of Theoretical and Applied Mechanics*, *51*(6), 1918-1926. https://doi.org/10.6052/0459-1879-19-231.

Marquis-Gravel, G., Redfors, B., Leon, M. B., & Généreux, P. (2016). Medical treatment of aortic stenosis. *Circulation*, *134*(22), 1766-1784. https://doi.org/10.1161/CIRCULATIONAHA.116.023997.

Pour, M. K., Nili-Ahmadabadi, M., Taherian, G., & Minaean, A. (2017). Experimental study of natural convective flow over a hot horizontal rhombus cylinder immersed in water via PIV technique. *Journal of Applied Fluid Mechanics*, *10*(2), 735-747. https://doi.org/10.18869/ACADPUB.JAFM.73.239.27300.

Qiang, Y., Duan, T. C., Zhang, M. Z., Qi, L., & Wei L. J. (2024). Experimental study of aortic BMHV flow characteristics under different physiological conditions using PIV. *Chinese Journal of Theoretical and Applied Mechanics*, *56*(6), 1807-1817. https://doi.org/10.6052/0459-1879-23-563.

Qiang, Y., Duan, T. C., Zhang, M. Z., Qi, L., Wei, L. J., & Wei, Z. Q. (2023a). Impact of bileaflet mechanical heart valve leaflet dysfunction on left ventricular blood flow: An experimental study. *Physics of Fluids*, *35*(9), 091909. https://doi.org/10.1063/5.0166451.

Qiang, Y., Zhang, Q., Qi, L., Duan, T. C., Zhang, M. Z., & Wei, L. J. (2023b). Research on the design and control method of cardiac pulsating flow analog drive motor. *Micromotors*, *56*(9), 26-32. https://doi.org/10.15934/j.cnki.micromotors.2023.09.009.

Qiu, Y. L., Chen, H. Y., Zeng, H. J., & Ji, L. (2022). Research on the way of adding tracer particles based on PIV experiment. *Chemical Engineering of Oil And*

Gas, *21*(3), 132-136. https://doi.org/10.3969/j.issn.1007-3426.2022.03.020.

Rajput, F. A., & Zeltser, R. (2023). *Aortic Valve Replacement.* StatPearls Publishing. PMID: 30725821.

Selmi, M., Chiu, W. C., Chivukula, V. K., Melisurgo, G., Beckman, G. A., Mahr, C., Aliseda, A., Votta, E., Redaelli, A., Slepian, M. J., Bluestein, D., Pappalardo, F., & Consolo, F. (2019). Blood damage in Left Ventricular Assist Devices: Pump thrombosis or system thrombosis? *The International Journal of Artificial Organs*, *42*(3), 113-124. https://doi.org/10.1177/0391398818806162.

Thielicke, W., & Sonntag, R. (2021). Particle image velocimetry for MATLAB: accuracy and enhanced algorithms in PIVlab. *Journal of Open Research Software*, *9*(1), 12. https://doi.org/10.5334/JORS.334.

Weinberg, E. J., Mack, P. J., Schoen, F. J., García-Cardeña, G., & Kaazempur Mofrad, M. R. (2010). Hemodynamic environments from opposing sides of human aortic valve leaflets evoke distinct endothelial phenotypes in vitro. *Cardiovascular Engineering*, *10*(1), 5-11. https://doi.org/10.1007/s10558-009-9089-9.

Xu, M. B., He, G., & Wen, J. (2022). Background interference removal algorithm for PIV preprocessing based on improved local otsu thresholding. *Chinese Journal of Biomedical Engineering (English Edition)*, *31*(4), 147-159. https://doi.org/10.1007/978-3-031-51455-5_24.

Yang, Y., Wang, Z. W., Chen, Z., Wang, X., Zhang, L. F., Li, S. N., Zheng, C. Y., Kang, Y. T., Jiang, L. L., Zhu, Z. H., & Gao, R. L. (2021). Current status and etiology of valvular heart disease in China: a population-based survey, *BMC Cardiovascular Disorders*, *21*(1), 1-9. https://doi.org/10.1186/s12872-021-02154-8.

Yoganathan, A. P., He, Z., & Jones, S. C. (2004). Fluid mechanics of heart valves. *Annual Review of Biomedical Engineering*, *6*(1), 331-362. https://doi.org/10.1146/annurev-fluid-122414-034314.